

Revealing Coupling Strength in Biological Plasmon-Exciton Systems through Far-Field Microscopy

Zhiyi Yuan

Nanyang Technological University

Shih-Hsiu Huang

National Cheng Kung University

Zhen Qiao

Chaoyang Gong

Nanyang Technological University

Yikai Liao

Nanyang Technological University

Munho Kim

Nanyang Technological University

Muhammad Birowosuto

Nanyang Technological University

Cuong Dang

Nanyang Technological University (NTU) <https://orcid.org/0000-0001-6183-4082>

Pin Chieh Wu

National Cheng Kung University <https://orcid.org/0000-0002-5781-9696>

Yu-Cheng Chen (✉ yucchen@ntu.edu.sg)

Nanyang Technological University <https://orcid.org/0000-0002-0008-5601>

Article

Keywords: optical coupling, plasmon-excitons, bioplasmonics, nanocavity, light-matter interactions, far-field imaging

Posted Date: October 20th, 2021

DOI: <https://doi.org/10.21203/rs.3.rs-944935/v1>

License:  This work is licensed under a Creative Commons Attribution 4.0 International License.

[Read Full License](#)

Revealing Coupling Strength in Biological Plasmon-Exciton Systems through Far-Field Microscopy

Zhiyi Yuan ¹⁺, Shih-Hsiu Huang ²⁺, Zhen Qiao ¹, Chaoyang Gong ¹, Yikai Liao ¹, Munho Kim ¹,
Muhammad D. Birowosuto ³, Cuong Dang ¹, Pin Chieh Wu^{2*}, Yu-Cheng Chen ^{14*}

¹ School of Electrical and Electronic Engineering, Nanyang Technological University, 50 Nanyang Avenue, 639798, Singapore

² Department of Photonics, National Cheng Kung University, Tainan 70101, Taiwan

³ CINTRA (CNRS–International–NTU-THALES-Research Alliances/UMI 3288), 50 Nanyang Drive, Singapore 637553, Singapore

⁴ School of Chemical and Biomedical Engineering, Nanyang Technological University, 62 Nanyang Drive, 637459, Singapore

⁺ *Equal Contribution*

^{*} *Correspondence Email:* pcwu@gs.ncku.edu.tw ; yucchen@ntu.edu.sg

Abstract

Optical coupling plays a pivotal role in nanophotonic systems, which can be divided into weak, intermediate, and strong coupling regimes. Determining coupling strength is, therefore, the key to understanding light-matter interactions. State-of-the-art approaches based on spectral-based measurements suffer from relatively large background noise or long accumulation time at single-cavity level, without being able to perform high-throughput characterizations. Here, we report an efficient far-field optical imaging technique that can directly reveal coupling strength in a plasmon-exciton systems, allowing multiple nanocavity emissions to be detected, imaged, and quantified individually. A light harvesting biomolecule- *chlorophyll a* was employed to study dynamic light-matter interactions in strongly-coupled bio-plasmonic nanocavities. Identification of coupling strength was achieved by extracting RGB values from dark-field images and enhancement factor from fluorescence images. Lastly, we demonstrate the ability to quantify excitons and subtle changes of weak coupling interactions in the bioplasmonic nanocavity. Our findings may deepen our understanding of fundamental science of light-matter interactions, paving new avenues toward real-world applications in quantum-based biosensing and imaging.

Keywords: optical coupling; plasmon-excitons; bioplasmonics; nanocavity; light-matter interactions; far-field imaging

Introduction

Light-matter interaction at the nanoscale lies at the heart of nanophotonics, offering tremendous possibilities in modern technology.¹⁻⁵ According to coupling strengths, light-matter interaction can be divided into three regimes: weak, intermediate, and strong coupling. In weak coupling regimes, spontaneous emission rate can be enhanced due to the modified photonic density of state (Purcell factor), which has been widely applied in nanophotonic devices and biosensing applications.⁶⁻¹⁰ In intermediate coupling regimes, a tiny dip begins to exhibit in the scattering or extinction spectrum (Fano interference) while the fluorescence intensity reaches its maximum value.¹¹⁻¹³ However, for strong coupling regimes, new hybridized eigenstates occur (Rabi splitting) when the energy exchange exceeds the dissipation rate.¹⁴ Owing to the part-matter and part-light characteristics of new hybridized eigenstates, either the material or photonic properties will be modified, leading to intense research effort in nanophotonics, quantum optics, and quantum chemistry.¹⁵⁻¹⁷ To date, strong coupling at room temperatures has been demonstrated in numerous cavities and excitonic systems. In terms of cavities, plasmon resonance cannot only squeeze light at the nanoscale to an ultrasmall mode volume but also provide a convenient route to manipulate light-matter interactions with high tunability.¹⁸⁻²⁰ For plasmon-exciton coupling, a wide range of materials can serve as excitonic systems, including semiconductor quantum dots,^{21,22} two-dimensional materials,²³⁻²⁵ organic molecules,²⁶⁻²⁸ and light-harvesting complexes.^{29,30} The realization of Rabi oscillation regime through strong coupling between plasmon-exciton can lead to a wide range of applications including electrically-tunable polaritons and low-threshold light amplification.³¹⁻³⁴

Although coupling regimes are directly or indirectly determined by many degrees of freedom (linewidth, coupling strength, spatial and spectral overlap, *etc.*), the coupling strength can directly reflect the interaction level between light and matter.¹⁴ As such, determining the coupling strength is the key to the understanding of light-matter interactions. In general, coupling strengths are determined by dark-field (DF) scattering spectra or time-resolved fluorescence (FL) spectra under plasmon-exciton coupling systems.^{35,36} However, spectral-based measurements suffer from relatively huge background noise or long accumulation time due to the sub-diffraction physical volume of plasmon-exciton systems, limiting their potential in real-world applications. In contrast to DF and FL spectra, the DF and FL emission far-field images can be captured based on the same optical path to achieve high-throughput detection and physical characterization. Nonetheless, coupling strength has never been directly quantified through far-field imaging.

In this study, we report an efficient far-field optical imaging technique that can directly reveal coupling strength in plasmon-exciton systems, enabling multiple light-matter interactions to be detected, imaged, and quantified individually. The overall concept is illustrated in Fig. 1. [Figure 1a](#) presents a film-coupled nanocube, where light-harvesting biomolecules- *chlorophyll a* (*chl a*) were embedded within the nanocavity formed between Ag nanocubes and a gold mirror. A thin layer of SiO₂ was deposited on the mirror to control the gap distance of nanocavity. Taking advantage of substantial electric field enhancement and ultrasmall mode volume ([Fig. 1b](#)), the optical properties of organic emitters and nanocavities are modified significantly. An example of a Ag nanocube is provided in [Fig. 1c](#). Both DF spectra and DF images were collected on a modified upright microscopic system. By splitting the original DF image into RGB color channels, the ratio of the total pixel intensity between red (R) to green (G) channel can be calculated (R/G ratio), as shown in [Fig. 1d](#). Details are provided in [Fig. S1a](#). Comparing to weakly coupled nanocavities, DF images produced by strongly coupled nanocavities exhibit lower R/G ratios ([Fig. 1d](#)). The relationship between the coupling strength g and R/G ratio reduction shows the potential quantitative capability of DF imaging, even at the weak coupling regime. Subsequently, we utilized FL imaging to characterize the relationship between the coupling strength and FL enhancement factor, which agrees well with the theoretical prediction. Finally, quantitative analysis of excitons in the weak coupling regime was demonstrated through far-field imaging. The key findings in our work not only can deepen and broaden our understanding of the physics of light-matter interactions but provide a novel tool to investigate bio-plasmon-exciton systems in quantum biosensing and bioimaging.

Results and Discussions

Design and concept of bio-plasmonic nanocavity

We first explored the correlation between R/G ratio and resonance energy in a pure plasmonic system without any gain molecules. By preparing silver (Ag) nanocubes on gold mirrors with different thickness of SiO₂ layer (3 nm, 5 nm, 9 nm), the distribution of resonance energy and linewidth can be adjusted ([Fig. S2a](#)). The resonance energy and linewidth of nanocavities can be calculated through the Lorentz peak fitting ([Fig. S1b and Supplementary Information section 1](#)). Note that only one prominent peak was observed in most cases rather than double peaks because

the total thickness of the spacer was at least 6 nm thickness (~3 nm polyvinylpyrrolidone coating). This feature has been reported by previous studies.^{37,38} As such, the correlation between the R/G ratio and resonance energy could be obtained through the DF image, as shown in Fig. S2b. Based on the single oscillator model and fitting efficiency of the color charge-coupled device (CCD) camera (Methods and Fig. S2c), the curved lines can be used to predict the relationship between the R/G ratio and resonance energy. The theoretical prediction is in accordance with the experimental results, demonstrating the capability to characterize resonance conditions in plasmonic nanocavities through DF images.³⁹

Next, *chla* molecules were embedded within the gap between Ag nanocube and gold mirror (with SiO₂ layer). To prove the *chla* coupled nanocavities can reach the regime of strong coupling regime, we theoretically estimate the coupling strength of *chla* within the nanocavities. According to the literature, we assume that most dipoles are oriented around 75° relative to the surface normal.⁴⁰ As such, the average coupling strength of a single *chla* molecule can be estimated as 0.52 meV. To reach the criteria of spectral splitting, $g > (\gamma_{pl} + \gamma_{chla})/4 \sim 50$ meV, the number of *chla* should exceed 9200 (Detailed calculations described in Supplementary Information section 8). Before Ag nanocube solution dropped cast on the mirror, a 2 μL of *chla* solution was drop cast on 1 cm² mirror with a concentration of 2 mM. The number of *chla* within a nanocavity is larger than 10000. As such, the *chla* coupled nanocavities can reach the regime of strong coupling regime. To exclude the effect of many other degrees of freedom (resonance energy, linewidth, environmental refractive index, orientation, and size of nanocube), a fixed nanocavity is required to investigate various coupling strengths. As such, the sample was illuminated with a UV light to change the coupling strength in a fixed nanocavity (see Methods).¹⁵ Throughout the study, photobleaching under UV illumination was employed to manipulate the number of excitons from *chla* molecules confined in nanocavities.

Investigation of strong coupling

To investigate strong coupling effects in *chla*-coupled nanocavities, we selected 6 individual nanocubes and compared its DF spectra before and after UV illumination in Figs. 2a and 2b, respectively (side by side). The resonance energy of nanocavities blueshifts from 1.80 eV to 1.94 eV, across the *chla* excitons. As shown in Fig. 2a, the dips at the absorption maximum of *chla* (~1.8977eV, Fig. S3) indicate a coherent coupling between the nanocavity and *chla* excitons. The

fitting curves of DF spectra were acquired through two coupled oscillators models (TCOM) (Supplementary Information section 2 and Method). Compared with coupled nanocavities in Fig. 2a, the DF images from uncoupled nanocavities (Fig. 2b) exhibited stronger red emissions (higher R/G ratio). For simplicity, all *chla* excitons involved in the coupling process can be treated as one oscillator with two energy levels. According to the TCOM, the upper and lower polariton energy branch can be written as:

$$\omega_{\pm} = \frac{1}{2}(\omega_{chla} + \omega_{pl}) \pm \frac{1}{2}\sqrt{4g^2 + \delta^2 - (\gamma_{pl} - \gamma_{chla})^2/4} \quad (1)$$

where ω_{pl} and ω_{chla} represent the resonance energy of plasmonic nanocavity and *chla* exciton, respectively.⁴¹ γ_{pl} and γ_{chla} are the linewidth of plasmonic nanocavity and *chla* exciton. $\delta = \omega_{pl} - \omega_{chla}$ is the detuning. The dispersion curve extracted from DF spectra in Figs. 2a-b is illustrated in Figure 2c, indicating an anticrossing behavior. According to the TCOM fitting, coupling strengths g and the upper (lower) polariton energy branch (ω_+ or ω_-) can be calculated. Besides, the resonance energy and linewidth of nanocavities can be calculated through the Lorentz model fitting from uncoupled nanocavities (Fig. 2b). Therefore, Rabi splitting is around 200 meV when the detuning $\delta = 0$, which is higher than the excitonic linewidth (~60 meV) and comparable with the nanocavity linewidth (150 to 350 meV). Figure 2d shows the coupling strengths extracted from the TCOM fitting. The averaged coupling strength equals 125 meV, which is larger than half of the Rabi splitting acquired. This is because the linewidth difference between nanocavity and *chla* reduces the Rabi splitting according to Eqn. 1. Unlike other studies based on the 2D materials,⁴² the coupling strength in different nanocavities shows relatively large fluctuation due to the large uncertainty of molecular orientation and spatial distribution of *chla* molecules. However, it remains challenging to confirm if the polariton system enters a strong coupling regime since intermediate coupling regimes (Fano resonance) also exhibit a splitting feature in DF spectra.^{43,44} To verify the strong coupling effect, we also measured the FL spectra to check if the polariton peak occurred. Splitting behavior was observed in FL spectra in part of *chla*-coupled nanocavities, as presented in Fig. S4. The FL spectra peak generated from uncoupled *chla* was located at 1.83 eV (679 nm), while strongly coupled *chla* showed a new peak at the lower polariton resonance energy. These observations in combination with the experimentally observed large energy splitting (larger than the excitonic linewidth) unambiguously confirm that strong coupling can be achieved in our system.

Effect of coupling strength on R/G ratio

Next, we demonstrate the influence of coupling strength on DF image in our plasmon-exciton system by quantitatively comparing the coupling strength g and R/G ratio change. To obtain different coupling strengths between coupled nanocavities, both the DF spectra and DF images were collected before and after the photobleaching process of *chla* molecules (Fig. 3a). Three individual nanocubes were selected based on different coupling strengths (weak, intermediate, and strong coupling). Figures 3b-d illustrate the corresponding DF spectra and DF images of *chla*-coupled nanocavities before and after UV illumination. By fitting with TCOM, the coupling strength can be extracted from the DF spectra (see Methods). Intuitively, different coupling strengths produce various features in optical spectrum, resulting in the change of far-field color imaging. Thus, the DF spectra and image in Fig. 3d showed less difference after the photobleaching process due to weak coupling.

To support our findings, a large number of DF spectra and images were also investigated (Figs. S5 and S6). The statistical results of *chla*-coupled nanocavities extracted from DF spectra and images through TCOM and image processing are presented in Fig. S7. By observing the DF images, more than 60% of the nanocavities exhibited a splitting behavior (Figs. S7d, e), while only 10% of samples have high cooperativity $C = g^2/\gamma_p\gamma_{chla} > 1$ (Fig. S7c).¹ The upper and lower polariton energy extracted from all the DF spectra based on Fig. S7 are plotted in Fig. 3e. A clear anticrossing behavior was observed in the dispersion curve.

As illustrated in Fig. 3f, the distribution of R/G ratio in the splitting regimes (orange spots) changed more significantly than no splitting (weak coupling) regimes (red spots). To exclude other parameters which may potentially influence the color of DF images, we analyzed the following factors. (1) Previous studies have reported that different focal planes may affect the DF spectra and image of plasmonic resonance.⁴⁵ Thus, we collected the DF spectra and images of single nanocavity under the different focal planes (Fig. S8). The fluctuation of R/G ratio can be avoided by taking the average value. (2) To rule out the potential effect of UV illumination on nanocavity resonance, we recorded the DF spectra and DF image of pure nanocavity (without *chla*) under UV illumination (Fig. S9). Although some metallic nanoparticles undergo structural changes during high-intensity illumination,⁴⁶ the structure of PVP-coated Ag nanocubes remains stable under light illumination, which is similar to the previous study.⁴⁷

Subsequently, the correlation between the coupling strength and normalized R/G ratio is plotted in Fig. 3g (normalized R/G = R/G ratio of coupled nanocavities to uncoupled nanocavities). Explicitly, the normalized R/G ratio decreases as the coupling strength increases, indicating that the change of DF image is mainly determined by the coupling between excitons and nanocavity. In addition, a simple theoretical analysis was conducted through TCOM and CCD efficiency at different wavelengths. As illustrated in Fig. S10a-c, spectral splitting begins to increase when the coupling strength increases. Due to different spectral responses of the color-CCD, an obvious color change could be observed from DF images during spectral splitting (Fig. S10d). However, the experimental normalized R/G ratio appears to be larger than that acquired from simulations in Fig. 3g.

For better understanding, numerical FDTD simulations were carried out to demonstrate the far-field projection of the coupled and uncoupled nanocavity. Figure S11a illustrates the geometry of our simulation, where the light source illuminates from an angle of incidence of $\theta_i=55^\circ$ (according to the objective's NA). The *chla* layer was modeled as a Lorentz model with oscillator strength $f = 0.43$ (Supplementary Information section 3). In this configuration, the scattering spectra from nanocavity exhibit splitting (Fig. S11b). Next, the collection efficiency of the objective can be calculated through the far-field patterns (XZ plane) produced by coupled and uncoupled nanocavities (Supplementary Information section 4). According to estimation, the collection efficiency under coupled and uncoupled nanocavity should be similar around 651nm (maximum R/G ratio of the CCD ~ 10); however, the collection efficiency of coupled nanocavity is higher than uncoupled nanocavity at 552 nm (minimum R/G ratio of CCD ~ 0.08). Compared with uncoupled nanocavities, coupled nanocavity receives more scattering signals from the green (G) channel, resulting in the further decrease of R/G ratio as the coupling strength increases.

Effect of coupling strength on fluorescence enhancement factor

It is noteworthy that slight changes among weakly coupled nanocavities are usually undetectable. For instance, no splitting was observed on the DF spectra in Fig. 3d. In contrast, this slight difference could be distinguished through R/G ratio acquired through DF images. Our findings indicate that DF images could potentially reveal coupling strengths where conventional spectra cannot. To gain profound insights into the effect of coupling strength on the plasmon-exciton systems, fluorescence emission (FL) images were recorded by the same optical configuration with

LED excitation (Fig. 4a). After the FL images were recorded, an area with 20×20 pixels was cropped containing the nanocube and its surrounding background (Fig. 4b). By analyzing the total pixel intensity of the cropped images, the average FL enhancement factor, $\langle EF \rangle$, can be calculated as:

$$\langle EF \rangle = \left(\frac{I_{cube}}{I_{background}} - 1 \right) \times \frac{S_{background}}{S_{cube}} \quad (2)$$

where I_{cube} is the total pixel intensity from the cropped image containing the nanocube, and $I_{background}$ is the total pixel intensity from the cropped image beside the nanocube.⁴⁸ $S_{background}$ defines the area of the cropped image ($\sim 0.9216 \mu\text{m}^2$), while S_{cube} denotes the area of the Ag nanocube ($\sim 0.075^2 \mu\text{m}^2$). Subsequently, $\langle EF \rangle$ values acquired by Eqn. 2 are presented in Fig. 4c to demonstrate the correlation between the coupling strength and $\langle EF \rangle$. A quadratic relation could still be identified along with coupling strength, given that the $\langle EF \rangle$ values were rather dispersive due to other degrees of freedom (e.g., resonance energy, the linewidth of nanocavity emission). Fig. 4c shows that the $\langle EF \rangle$ increases proportionally with the coupling strength below a coupling strength of 90 meV. However, $\langle EF \rangle$ values began to decrease when coupling strength reached beyond 90 meV. This is due to the breakdown of Purcell factor when light-matter interactions in nanocavities become strong enough.^{49,50}

Again, numerical FDTD simulation was delivered to demonstrate the influence of coupling strength on Purcell effect. Fig. S12a shows the simulated configuration of Purcell effect detection. As the oscillator strength f increases, the extinction spectra of nanocavity display a splitting behavior (Fig. S12b). Note that the effective oscillator strength f is proportional to the number of excitons N_{ex} , while N_{ex} is proportional to the square of coupling strength g (Supplementary Information section 5). By controlling the position and orientation of dipole within the nanocavity, the Purcell factor can be compared under different oscillator strength f , as shown in Fig. S12c. Interestingly, the relationship between the square root of oscillator strength f and Purcell factor also follows the quadratic relation, which is similar to Fig. 4c. The saturation of Purcell factor or $\langle EF \rangle$ can be verified by the theoretical analysis in Supplementary Information section 6.

However, $\langle EF \rangle$ depends on many factors and thus it is not directly equal to Purcell factor. According to the previous studies, $\langle EF \rangle$ can also be written as:⁴⁰

$$EF = \frac{\eta \gamma_{ex}(r, \theta) QY(r)}{\eta_0 \gamma_{ex}^0(\theta) QY_0} = \frac{\eta \gamma_{ex}(r, \theta)}{\eta_0 \gamma_{ex}^0(\theta)} \frac{\gamma_{rad} / \gamma_{rad}^0}{QY_0 (\gamma_{rad} / \gamma_{rad}^0 + \gamma_{loss} / \gamma_{rad}^0) + (1 - QY_0)} \quad (3)$$

where $\gamma_{sp} = \gamma_{rad} + \gamma_{loss}$ represents the Purcell factor, γ_{rad} and γ_{loss} are the radiative rate and loss rate due to metal quenching, respectively. η and η_0 are the collection efficiency of dipole within and without the nanocavity, respectively. γ_{ex} and γ_{ex}^0 denote the excitation rate of dipole within and without the nanocavity. QY_0 is the intrinsic quantum yield of *chla* molecules. (Detailed calculations described in [Supplementary Information section 7](#)).

To obtain the excitation rate enhancement at the excitation wavelength, we plotted each component of electric field distribution (E_x , E_y , E_z) in the nanocavity in [Fig. S13](#). Note that E_z (perpendicular to the gold mirror) is the dominant component within nanocavity which also verifies the strong near-field coupling between the topmost nanocube and the gold mirror. Therefore, the orientation of dipole plays a crucial role in spontaneous emission. [Fig. S14](#) plots the radiation pattern of dipole within the nanocavity and on the gold mirror, showing the collection efficiency enhancement within the nanocavity (64% and 40%). To calculate $\langle EF \rangle$, maps of enhancement of the spontaneous emission rate (Purcell effect $\gamma_{sp}/\gamma_{rad}^0$) as a function of the position under nanocube was performed. As shown in [Fig. 4d](#), the largest Purcell factor occurs for emitters located near the edge of nanocavity (~ 7000). Additionally, maps of radiative emission rate ($\gamma_{rad}/\gamma_{rad}^0$) and quantum yield (QY/QY_0) for vertical orientation dipole (0°) were also calculated, as displayed in [Figs. 4e-f](#). According to simulation results, the average Purcell factor within the nanocavity $F_p = \iint_{x,y} F_p(x,y)/S$ can be calculated as 2300. However, the average orientation of *chla* molecules cannot be vertical without any chemical process. For brevity, we assume that the average orientation angle of the dipole is around 75° with respect to the z -direction.⁴⁰ Under this orientation, both the excitation rate enhancement and Purcell effect decrease since the orientation of the electric fields are mainly vertical in the nanocavity ([Fig. S15](#)). According to the above theoretical calculation, the simulated $\langle EF \rangle$ can be estimated as 22.6 for 75° dipoles and 466 for 0° dipoles. These calculated values are much lower than the results in [Fig. 4c](#) since the effect of coupling strength was not considered, verifying that stronger coupling strength can also enhance overall $\langle EF \rangle$.

Dynamic imaging of coupling strength through DF and FL images

The above-described results indicate a critical feature in plasmon-exciton systems; that is, light-matter interactions at the nanoscale can make a huge impact on its far-field image. Moving forward, here we investigated the dynamic changes of *chla*-coupled nanocavities as the number of

excitons decreases through photobleaching process. A set of strongly coupled nanocavity and weakly coupled nanocavity was prepared and compared in Fig. 5 (top row and bottom row, respectively). Figures 5a and 5b present the DF spectra under a strong coupling and a weak coupling system. In contrast to the weak coupling system, the DF spectra of the strong coupling system show a noticeable splitting at the beginning (Fig. 5a). As the UV illumination time increased, the splitting decreased rapidly and remained stable with only one broad peak left after one minute. Oppositely in Fig. 5b, no splitting in DF spectra was observed for weak coupling system; the peak remains similar and stable. The corresponding DF images as well as FL images were both captured and presented in Figs. 5c and 5d, respectively. As such, the R/G ratio and $\langle EF \rangle$ could be extracted. The R/G ratio in DF image increases while $\langle EF \rangle$ in FL images decreases since the effective *chl*a concentration decreases as the UV illumination (Figs. 5c,d).

Combining DF spectra with its corresponding DF images, the coupling strength for strong and weak coupling system can be quantified dynamically through R/G ratio, as shown in Figs. 5e and 5f, respectively. In the first 1.5 minutes, the coupling strength of strong coupling system reduces abruptly while the R/G ratio rises suddenly. However, the R/G ratio increased much slower when the spectral splitting cannot be detected anymore (Fig. 5e), which is similar to weak coupling system (Fig. 5f).

Additionally, we surprisingly found that $\langle EF \rangle$ extracted from the FL images in Figs. 5c and 5d possess a strong correlation with coupling strength. In the strong coupling regime, Fig. 5g shows the extracted $\langle EF \rangle$ and normalized R/G ratio as a function of coupling strength. A high correlation between R/G ratio and coupling strength, as well as $\langle EF \rangle$ and coupling strength, was discovered. In the weak coupling regime, the exact value of coupling strength was not able to be calculated. However, our results in Fig. 5h show that the slight dynamic changes of the weak coupling strength could still be analyzed by R/G ratio and $\langle EF \rangle$ through far-field imaging. It is noteworthy that it is nearly impossible to identify the different extent of coupling strength in the weak coupling regime under conventional spectral-based measurement.³⁵

Quantitative analysis of excitons in bio-plasmonic nanocavity

Finally, we demonstrate the ability to directly quantify weak coupling interactions through far-field imaging. Herein nanocavities sandwiched with different concentrations of *chl*a molecules were prepared and compared under FL microscopy (Figs. 6a-6d) and DF microscopy (Figs. 6e-

6h). Several nanocubes could be imaged at the same time through FL imaging and DF imaging, while each dashed circle represents a single nanocube with *chla* molecules beneath. Although DF and FL images were recorded by different CCDs, the relative position of nanocavities remains unchanged. Figures 6a-6d show that the contrast of FL images increases rapidly as the number of *chla* molecules increases, indicating that the $\langle EF \rangle$ increases as the *chla* concentration increases. In comparison, the DF images corresponding to Figs. 6a-6d are provided in Figs. 6e-6h. By extracting the R/G ratio from Figs. 6e-6h, the relationship between R/G ratio and $\langle EF \rangle$ was acquired in Fig. 6i. The statistical results of R/G ratio and $\langle EF \rangle$ are also plotted in Fig. S16. As one can see, the mean values of R/G ratio decrease as the number of *chla* molecules increases (2.91, 2.85, 2.55, 2.35), while $\langle EF \rangle$ increases as the number of *chla* molecules increases (11, 36, 147, 1567).

In theory, coupling strength g is proportional to the square root of the effective number of excitons N_{ex} . Considering the spatial difference of light-matter interactions, the square of coupling strength $g^2 = \sum_i g_i^2(r_i)$ is the summary of the square of the local coupling strength.⁵¹ As such, the number of excitons does not represent the molecule concentration since the coupling strength of each molecule is different in the different spatial. For brevity, the number of excitons is roughly proportional to the number of *chla* molecules if we assume the whole nanocube is one unit. Similar to $\langle EF \rangle$, the quadratic relationship between the R/G ratio and the square root of *chla* molecule number agrees well with our above-mentioned results (Figures 6j-k). The $\langle EF \rangle$ for nanocavities containing the lowest number of *chla* molecules is around 11 (~ single molecules level), which is close to the previous simulation prediction (22.6). Owing to higher background noise from FL imaging under extremely low *chla* concentrations, the experimental $\langle EF \rangle$ value is lower than the simulation values. Note that most nanocavities did not enter the strong coupling regime even with 7000 *chla* molecules.

According to the theoretical estimation in Supplementary Information section 8, we can obtain the maximum coupling strength produced by a single *chla* molecule (~2 meV). Considering the dot product between the electric field and the dipole moment, the average coupling strength of a single *chla* molecule can be estimated as 0.52 meV when the average orientation angle of the dipole is around 75° .⁴⁰ The expected coupling strengths of nanocavities containing 70/700/7000 *chla* molecules are 4/14/44 meV, which are lower than the criteria of Rabi splitting ($4g > \gamma_{pl} + \gamma_{chla} \sim 50$ meV). Experimentally, the normalized R/G ratio (by using 7 *chla* molecules as a base

reference) (0.98/0.87/0.81) is lower than the theoretical fitting in Fig. 3g (0.98/0.96/0.88). This deviation is mainly due to the local refractive index difference and cavity gap thickness difference under various *chla* concentrations (Supplementary Information section 8). Note that according to our fitting results in Fig. 4c, the $\langle EF \rangle$ at 40 meV (1200) is close to the experimental result (1567).

Conclusion

To summarize, we explored light-matter interactions at the nanoscale in the plasmon-exciton systems by using a light harvesting molecule- *chlorophyll a* as an example. Thanks to the ultrasmall mode volume of nanocavities, strong coupling can be achieved in bio-plasmonic nanocavities. The anticrossing behavior of the dispersion curve extracted from DF spectra associated with large energy splitting verifies the realization of strong coupling regime. Our findings demonstrate that coupling strength can be directly revealed by far-field imaging techniques. According to the simulated and experimental results, we discovered that coupling strength could affect the R/G ratio in DF images and the enhancement factor in FL images. Lastly, quantitative analysis in the weak coupling regime was performed based on far-field images. A high correlation between R/G ratio and the square root of the number of molecules, as well as $\langle EF \rangle$ and the square root of the number of molecules was confirmed. It is also noteworthy that the spatial mode modifications of the DF image have been recently observed in the strong coupling regime.⁵² Combining with our investigation, far-field imaging may serve as a direct and effective tool for exploring fundamental science and light-matter interactions in plasmon-exciton systems.

Quantum-based technology, which takes advantage of plasmon-exciton systems, is also regarded as one of the most promising candidates for biosensing.^{53,54} A plethora of studies have demonstrated the extremely high sensitivity in the strong coupling quantum regime. Given the high-performance quantum sensors may provide, current techniques are still limited to single-cavity detection, hindering it from real-world applications. This is mainly due to the relatively huge background noise or long accumulation time during spectral-based measurements. The role of chlorophyll molecule in this study can be simply replaced by any other biomolecules and even dynamic biological interactions to form a biological plasmon-exciton system. The proposed concept of imaging-based, spectrometer-less approach, therefore, provides an alternative for future application in quantum biosensing.

Methods

Numerical simulation

The 3D numerical simulations are performed by Lumerical Finite-Difference-Time-Domain (FDTD) Solutions v8. 24. The structure was modeled as a silver nanocube with a side length of 60 – 90 nm on top of a gold layer, a flat infinite 3nm thick SiO₂ layer, and 1-2nm thick Chlorophyll-a layer in between. The dielectric function of silver is taken from Johnson and Christy. The silver nanocube was illuminated with p-polarized plane wave (TFSF source) from an angle of incidence of $\theta_i=55^\circ$. To calculate the x,y,z components of electric field distribution at emitter excitation wavelength within nanocavity, the p-polarized plane wave from an angle of incidence of $\theta_i=0^\circ$ was selected. The inbuilt sweep parameter was used to include the incident wavelengths ranging from 400 to 800 nm.

For simulations, the effective dielectric function of chlorophyll-a was calculated using a classical Lorentz model:

$$\varepsilon_{chla} = \varepsilon + \frac{f \omega_{chla}^2}{\omega_{chla}^2 - \omega^2 - i\omega\gamma_{chla}}$$

where $\varepsilon = 2.31$ is the dielectric constant of *chlorophyll-a* molecule,⁵⁵ $\omega_{chla} = 2.877 \times 10^{15}$ (1.8977 eV) is the absorption maximum of *chla*, $\gamma_{chla} = 9.098 \times 10^{13}$ (0.06 eV) is the linewidth of *chla*. f represents the reduced oscillator strength which was calculated in SI section 1.

A silver nanocube with side length of 75 nm was used to compute the spontaneous emission enhancement, the radiative enhancement, and the quantum efficiency enhancement. The *chla* molecule was modeled as electrical dipole emitting from 640 nm to 740 nm. The numerical computation was calculated by varying the position of the dipole emitter on a discrete 15×15 grid placed beneath the nanocube (mesh at *xy* plane = 5 nm). The four-fold symmetry of the NPA was used to reduce the necessary number of simulations. The radiative and non-radiative rates were obtained by integrating the total power radiated out of the entire domain and absorbed from the plasmonic system, which can be calculated by FDTD. To calculate the scattering spectra and Purcell effect (Fig. S11 and S12) under the different oscillator strengths, we used a silver nanocube with a side length of 70 nm.

Optical measurements

Darkfield spectra were recorded on a modified upright microscopic system (Nikon Ni2). Samples are illuminated with a focused white light (halogen) source at 55° . The scattered light was collected through a 50× darkfield objective (NA=0.8) and was separated by a beam splitter and incident into a cooled spectrometer (Andor Kymera 328i) and charge-coupled device camera (DS-Fi3 color CCD). For all the DF image collections, the color channel setup was fixed (red channel ×2, green channel ×1). Integration time was 0.5s but accumulated 20-30 times for each spectrum to increase the signal-to-noise ratio. All measured dark-field spectra were corrected for background scattering and normalized by the intensity of the white light using the following equation.⁵⁶

$$I_{sca} = \frac{I_{sample} - I_{background}}{I_{lamp} - I_{dark}}$$

where I_{sca} is the spectrum of the sample (nanocavity), $I_{background}$ is the background spectrum near the sample, I_{lamp} is the spectrum of halogen light source, and I_{dark} is the detector dark count spectrum. To obtain the fluorescence images of *chlorophyll-a*, LED with filter (600–640 nm) was selected as light source. The fluorescence images were collected through a 50× objective (NA=0.8)

and charge-coupled device camera (Newton 970 CCD) with a bandpass filter (690/50 nm).

DF spectra fitting

Before the fitting, all the DF spectra $I_{sca}(\omega)$ were normalized by dividing the maximum value. DF spectra of pure nanocavities were fitted by Lorentz oscillation resonance:

$$I_{sca}(\omega) \propto a + 2 \times \frac{b}{\pi} \times \frac{\gamma_{pl}}{(4 \times (\omega - \omega_{pl})^2 + \gamma_{pl}^2)}$$

where γ and ω_1 represent the linewidth and energy of the plasmon resonance, respectively. From the above formula, we can obtain the resonance energy and linewidth of nanocavity.

DF spectra of *chla* coupled nanocavities were fitted by two oscillators models:

$$I_{sca}(\omega) \propto \omega^4 |c_1|^2 \propto \omega^4 \left| \frac{\omega_{chla}^2 - \omega^2 + i\gamma_{chla}\omega}{(\omega_{chla}^2 - \omega^2 + i\gamma_{chla}\omega)(\omega_{pl}^2 - \omega^2 + i\gamma_{pl}\omega) - g^2} \right|^2$$

From the above formula, we can obtain the coupling strength, resonance energy and linewidth of nanocavity.

Fitting the quantum efficiency of CCD at different wavelengths

From the website of CCD (DS-Fi3 Nikon), we can obtain the quantum efficiency of different channels (R/G/B) at different wavelengths. Here we only care about the red (R) channel and green (G) channel since the plasmonic nanocavity resonance wavelength is longer than 600 nm. Besides, the efficiency of red channel should be multiplied by a factor of 2 due to CCD parameter settings.

Sample preparation

Ag nanocubes were purchased from nanoComsix (75 nm \pm 10 nm). Each nanocube was coated with Ployvinylpyrrolidone (PVP) \sim 3 nm. A 5-nm-thick Cr layer, 100-nm-thick Au mirror, and 1-nm-thick Cr layer were firstly deposited on a silicon substrate via the thermal evaporator. The deposition rate for Cr and Au is 0.6 angstrom/s and 1.0 angstrom/s, respectively. The Cr layers were used to increase the adhesion between silicon substrate (or SiO₂ spacer) and Au mirror. A dielectric spacer SiO₂ with designed thickness was then deposited by a magnetron sputtering machine.

Chlorophyll-a (Sigma-Aldrich #C5753) was dissolved in ethanol with 2 mM concentrations. A 2- μ L of *chlorophyll-a* solution was drop cast on the mirror and dried in dark air to prevent photobleaching. Subsequently, a diluted Ag nanocube solution (1:2500) dropped cast on the mirror and dried in dark. Note that in Fig. 6, an estimation of 7/70/700/7000 molecules were embedded within 75 nm side length Ag nanocube. This is because 2- μ L of *chlorophyll-a* solution was drop cast on 1 cm² mirror with a concentration of 0.1/1/10/100 μ M, respectively.

Acknowledgments

Y.C.C. would especially like to thank the financial support from A*STAR- Singapore under its AME IRG- Grant (No. A20E5c0085). Y.C.C. would also like to thank Dr. Muhammad Faeyz Karim for his support on the server and equipment. P.C.W. acknowledges the support from Ministry of Science and Technology (MOST), Taiwan (Grant number: 107-2923-M-006-004-MY3; 108-2112-M-006-021-MY3; 110-2124-M-006-004), and in part from the Higher Education

Sprout Project of Ministry of Education (MOE) to the Headquarters of University Advancement at National Cheng Kung University (NCKU). P.C.W. also acknowledges the support from Ministry of Education (Yushan Young Scholar Program), Taiwan.

Supplementary Information

Supplementary Information is available online.

Author Contributions

Yu-Cheng Chen and Zhiyi Yuan formulated the idea behind the study. Zhiyi Yuan and Yu-Cheng Chen designed the experiments. Zhiyi Yuan and Muhammad D. Birowosuto performed the experiments. Zhiyi Yuan and Zhen Qiao and Chaoyang Gong conducted the data analysis. Zhiyi Yuan and Muhammad D. Birowosuto performed the numerical simulations. Shih-Hsiu Huang and Pin Chieh Wu fabricated the gold mirror. Munho Kim and Yikai Liao provided support on SEM images. Zhiyi Yuan and Yu-Cheng Chen wrote the manuscript. Cuong Dang, Pin Chieh Wu, and Yu-Cheng Chen supervised the whole study.

Reference

- 1 Pelton, M., Storm, S. D. & Leng, H. Strong coupling of emitters to single plasmonic nanoparticles: exciton-induced transparency and Rabi splitting. *Nanoscale* **11**, 14540-14552 (2019).
- 2 Chikkaraddy, R. *et al.* Single-molecule strong coupling at room temperature in plasmonic nanocavities. *Nature* **535**, 127-130 (2016).
- 3 Mueller, N. S. *et al.* Deep strong light–matter coupling in plasmonic nanoparticle crystals. *Nature* **583**, 780-784 (2020).
- 4 Rajabali, S. *et al.* Polaritonic nonlocality in light–matter interaction. *Nat. Photonics*, 1-6 (2021).
- 5 Benz, F. *et al.* Single-molecule optomechanics in “picocavities”. *Science* **354**, 726-729 (2016).
- 6 Wu, Y. *et al.* Upconversion superburst with sub-2 μ s lifetime. *Nat. Nanotechnol.* **14**, 1110-1115 (2019).
- 7 Cruz, D. F. *et al.* Ultrabright Fluorescence Readout of an Inkjet-Printed Immunoassay Using Plasmonic Nanogap Cavities. *Nano Lett.* **20**, 4330-4336 (2020).
- 8 Hoang, T. B. *et al.* Ultrafast spontaneous emission source using plasmonic nanoantennas. *Nat. Commun.* **6**, 1-7 (2015).
- 9 Hoang, T. B., Akselrod, G. M. & Mikkelsen, M. H. Ultrafast room-temperature single photon emission from quantum dots coupled to plasmonic nanocavities. *Nano Lett.* **16**, 270-275 (2016).
- 10 Zhang, F. L. *et al.* Elucidating Molecule–Plasmon Interactions in Nanocavities with 2 nm Spatial Resolution and at the Single - Molecule Level. *Angew. Chem. Int. Ed.* **131**, 12261-12265 (2019).
- 11 Sun, J. *et al.* Light-emitting plexciton: exploiting plasmon–exciton interaction in the intermediate coupling regime. *ACS nano* **12**, 10393-10402 (2018).
- 12 Wang, M. *et al.* Dark - Exciton - Mediated Fano Resonance from a Single Gold Nanostructure on Monolayer WS₂ at Room Temperature. *Small* **15**, 1900982 (2019).
- 13 Zhang, Y. *et al.* Sub-nanometre control of the coherent interaction between a single molecule and a plasmonic nanocavity. *Nat. Commun.* **8**, 1-7 (2017).
- 14 Khitrova, G., Gibbs, H., Kira, M., Koch, S. W. & Scherer, A. Vacuum Rabi splitting in semiconductors. *Nat. Phys.* **2**, 81-90 (2006).
- 15 Munkhbat, B., Wersäll, M., Baranov, D. G., Antosiewicz, T. J. & Shegai, T. Suppression of photo-oxidation of organic chromophores by strong coupling to plasmonic nanoantennas. *Sci. Adv.* **4** (2018).
- 16 Ojambati, O. S. *et al.* Quantum electrodynamics at room temperature coupling a single vibrating molecule with a plasmonic nanocavity. *Nat. Commun.* **10**, 1-7 (2019).
- 17 Silva, R., Del Pino, J., García-Vidal, F. J. & Feist, J. Polaritonic molecular clock for all-optical ultrafast imaging of wavepacket dynamics without probe pulses. *Nat. Commun.* **11**, 1-8 (2020).
- 18 Santhosh, K., Bitton, O., Chuntanov, L. & Haran, G. Vacuum Rabi splitting in a plasmonic cavity at the single quantum emitter limit. *Nat. Commun.* **7**, 1-5 (2016).
- 19 Kleemann, M.-E. *et al.* Strong-coupling of WSe₂ in ultra-compact plasmonic nanocavities at room temperature. *Nat. Commun.* **8**, 1-7 (2017).

- 20 Hou, S. *et al.* Manipulating Coherent Light–Matter Interaction: Continuous Transition between Strong Coupling and Weak Coupling in MoS₂ Monolayer Coupled with Plasmonic Nanocavities. *Adv. Opt. Mater.* **7**, 1900857 (2019).
- 21 Yadav, R. K. *et al.* Room temperature weak-to-strong coupling and the emergence of collective emission from quantum dots coupled to plasmonic arrays. *ACS nano* **14**, 7347-7357 (2020).
- 22 Gupta, S. N. *et al.* Complex plasmon-exciton dynamics revealed through quantum dot light emission in a nanocavity. *Nat. Commun.* **12**, 1-9 (2021).
- 23 Qin, J. *et al.* Revealing strong plasmon-exciton coupling between nanogap resonators and two-dimensional semiconductors at ambient conditions. *Phys. Rev. Lett.* **124**, 063902 (2020).
- 24 Cuadra, J. *et al.* Observation of tunable charged exciton polaritons in hybrid monolayer WS₂– plasmonic nanoantenna system. *Nano Lett.* **18**, 1777-1785 (2018).
- 25 Kleemann, M.-E. *et al.* Strong-coupling of WSe₂ in ultra-compact plasmonic nanocavities at room temperature. *Nat. Commun.* **8**, 1-7 (2017).
- 26 Zengin, G. *et al.* Realizing strong light-matter interactions between single-nanoparticle plasmons and molecular excitons at ambient conditions. *Phys. Rev. Lett.* **114**, 157401 (2015).
- 27 Huang, J., Traverso, A. J., Yang, G. & Mikkelsen, M. H. Real-time tunable strong coupling: From individual nanocavities to metasurfaces. *ACS Photonics* **6**, 838-843 (2019).
- 28 Zengin, G. *et al.* Approaching the strong coupling limit in single plasmonic nanorods interacting with J-aggregates. *Sci. Rep.* **3**, 1-8 (2013).
- 29 Tsargorodska, A. *et al.* Strong coupling of localized surface plasmons to excitons in light-harvesting complexes. *Nano Lett.* **16**, 6850-6856 (2016).
- 30 Coles, D. M. *et al.* Strong coupling between chlorosomes of photosynthetic bacteria and a confined optical cavity mode. *Nat. Commun.* **5**, 1-9 (2014).
- 31 Flatten, L. C. *et al.* Electrically tunable organic–inorganic hybrid polaritons with monolayer WS₂. *Nat. Commun.* **8**, 1-5 (2017).
- 32 Lim, H.-T., Togan, E., Kroner, M., Miguel-Sanchez, J. & Imamoğlu, A. Electrically tunable artificial gauge potential for polaritons. *Nat. Commun.* **8**, 1-6 (2017).
- 33 Dietrich, C. P. *et al.* An Exciton-Polariton Laser Based on Biologically Produced Fluorescent Protein. *Sci. Adv.* **2**, e1600666 (2016).
- 34 Wei, M. *et al.* Low-threshold polariton lasing in a highly disordered conjugated polymer. *Optica* **6**, 1124-1129 (2019).
- 35 Leng, H., Szychowski, B., Daniel, M.-C. & Pelton, M. Strong coupling and induced transparency at room temperature with single quantum dots and gap plasmons. *Nat. Commun.* **9**, 1-7 (2018).
- 36 Singh, A., de Roque, P. M., Calbris, G., Hugall, J. T. & van Hulst, N. F. Nanoscale mapping and control of antenna-coupling strength for bright single photon sources. *Nano Lett.* **18**, 2538-2544 (2018).
- 37 Lassiter, J. B. *et al.* Plasmonic waveguide modes of film-coupled metallic nanocubes. *Nano Lett.* **13**, 5866-5872 (2013).
- 38 Chikkaraddy, R. *et al.* How ultranarrow gap symmetries control plasmonic nanocavity modes: from cubes to spheres in the nanoparticle-on-mirror. *ACS Photonics* **4**, 469-475 (2017).

- 39 Gu, Z., Jing, C., Ying, Y.-L., He, P. & Long, Y.-T. In situ high throughput scattering light
analysis of single plasmonic nanoparticles in living cells. *Theranostics* **5**, 188 (2015).
- 40 Akselrod, G. M. *et al.* Probing the mechanisms of large Purcell enhancement in plasmonic
nanoantennas. *Nat. Photonics* **8**, 835-840 (2014).
- 41 Chikkaraddy, R. *et al.* Mapping nanoscale hotspots with single-molecule emitters
assembled into plasmonic nanocavities using DNA origami. *Nano Lett.* **18**, 405-411
(2018).
- 42 Yu, J. *et al.* Strong plasmon-Wannier Mott exciton interaction with high aspect ratio
colloidal quantum wells. *Matter* **2**, 1550-1563 (2020).
- 43 Wersall, M., Cuadra, J., Antosiewicz, T. J., Balci, S. & Shegai, T. Observation of mode
splitting in photoluminescence of individual plasmonic nanoparticles strongly coupled to
molecular excitons. *Nano Lett.* **17**, 551-558 (2017).
- 44 Wersäll, M. *et al.* Correlative dark-field and photoluminescence spectroscopy of individual
plasmon–molecule hybrid nanostructures in a strong coupling regime. *ACS photonics* **6**,
2570-2576 (2019).
- 45 De Nijs, B. *et al.* Unfolding the contents of sub-nm plasmonic gaps using normalising
plasmon resonance spectroscopy. *Faraday Discuss.* **178**, 185-193 (2015).
- 46 Mertens, J., Kleemann, M.-E., Chikkaraddy, R., Narang, P. & Baumberg, J. J. How light
is emitted by plasmonic metals. *Nano Lett.* **17**, 2568-2574 (2017).
- 47 Xomalis, A. *et al.* Controlling optically driven atomic migration using crystal-facet control
in plasmonic nanocavities. *ACS nano* **14**, 10562-10568 (2020).
- 48 Akselrod, G. M. *et al.* Leveraging nanocavity harmonics for control of optical processes in
2D semiconductors. *Nano Lett.* **15**, 3578-3584 (2015).
- 49 De Liberato, S. Light-matter decoupling in the deep strong coupling regime: The
breakdown of the purcell effect. *Phys. Rev. Lett.* **112**, 016401 (2014).
- 50 Ciuti, C. & Carusotto, I. Input-output theory of cavities in the ultrastrong coupling regime:
The case of time-independent cavity parameters. *Phys. Rev. A* **74**, 033811 (2006).
- 51 Liu, R. *et al.* Strong light-matter interactions in single open plasmonic nanocavities at the
quantum optics limit. *Phys. Rev. Lett.* **118**, 237401 (2017).
- 52 Chen, X. *et al.* Mode modification of plasmonic gap resonances induced by strong coupling
with molecular excitons. *Nano Lett.* **17**, 3246-3251 (2017).
- 53 Kongsuwan, N. *et al.* Quantum plasmonic immunoassay sensing. *Nano Lett.* **19**, 5853-5861
(2019).
- 54 Park, J.-H. *et al.* Symmetry-breaking-induced plasmonic exceptional points and nanoscale
sensing. *Nat. Phys.* **16**, 462-468 (2020).
- 55 Aas, E. Refractive index of phytoplankton derived from its metabolite composition. *J.*
Plankton Res. **18**, 2223-2249 (1996).
- 56 Hartsfield, T. *et al.* Single quantum dot controls a plasmonic cavity's scattering and
anisotropy. *Proc. Natl. Acad. Sci. U.S.A.* **112**, 12288-12292 (2015).

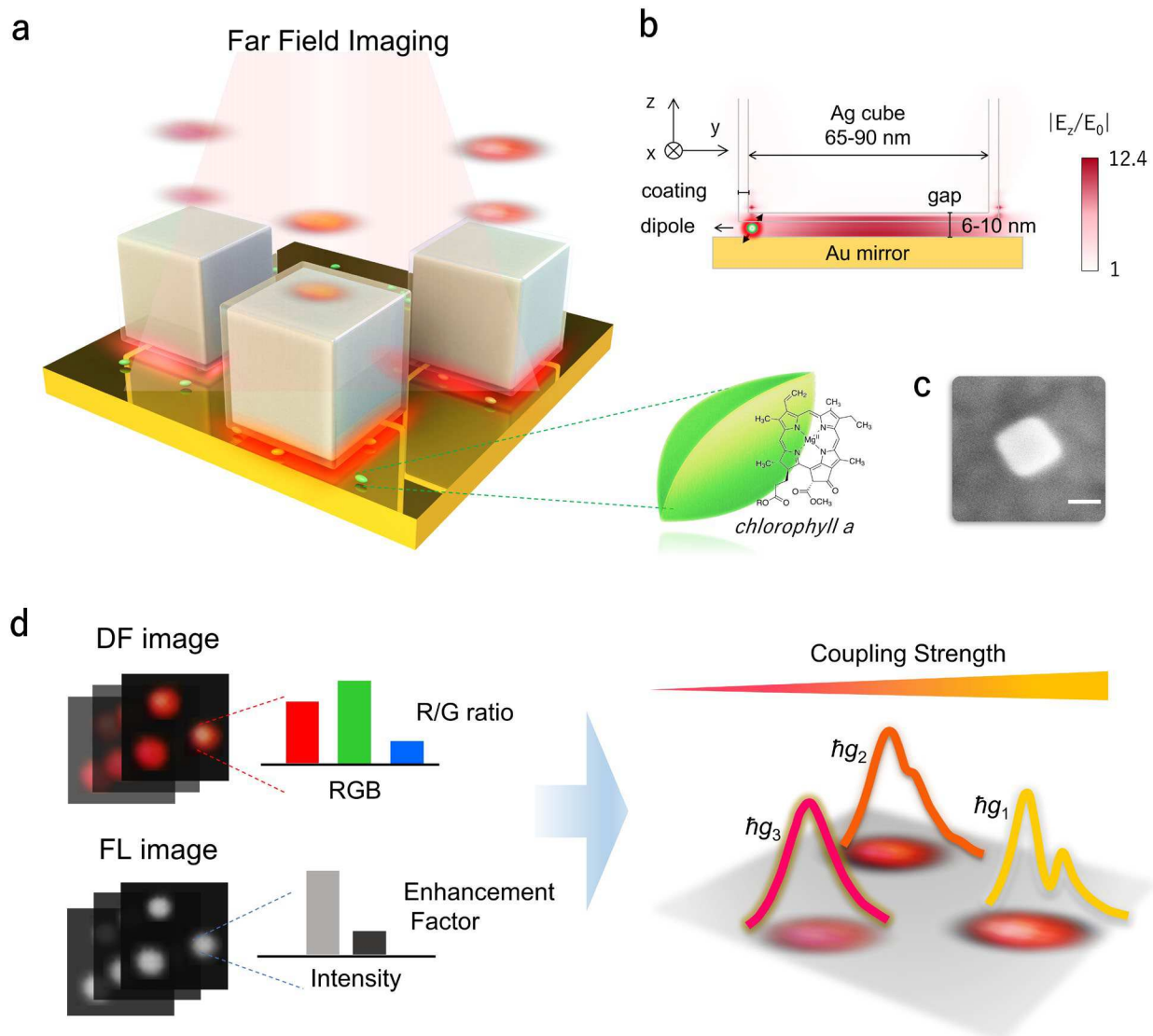


Figure 1. Concept of imaging coupling strength through far-field microscopy. (a) Schematic illustration of bioplasmonic nanocavity, where Ag nanocubes on the top of gold mirror separated by a gap layer (6-10 nm) containing *chlorophyll-a* molecules (green dots). Inset: molecular formula of *chlorophyll-a* (*chla*) molecule extracted from leaves. **(b)** yz cross-section of a plasmonic nanocavity with the simulated electric field distribution under the dark-field (DF) excitation ($\sim 55^\circ$ relative to the surface normal z -axis) at the absorption maximum wavelength (655 nm) of *chla*. The vertical direction (z) of the electric field is dominant on the gap electric field. **(c)** Scanning electron microscope (SEM) image of a single Ag nanocube. Scale bar, 50 nm. **(d)** Far-field images (DF & FL image) from the nanocavity under the different coupling strengths were imaged and studied. RGB values extracted from DF images and $\langle EF \rangle$ factor extracted from FL images were applied to characterize optical coupling strength.

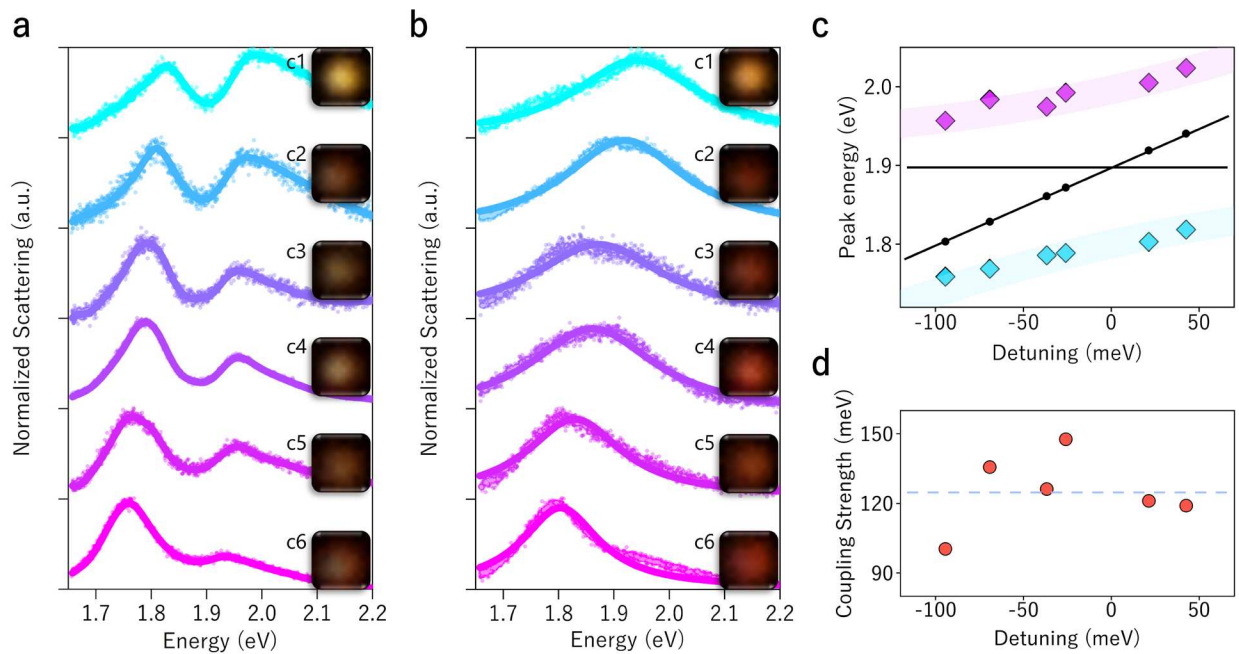


Figure 2. Strong coupling achieved in *chla*-coupled nanocavity. (a) Normalized scattering spectra (dots) for 6 independent nanocavities coupled with *chla*, with 3 nm SiO₂ layer. Inset CCD images: DF scattering images of different nanocavities coupled with *chla*. Curved lines are fitting with two coupled oscillators model. (b) Normalized scattering spectra (dots) for different nanocavities in (a) after the UV illumination. Inset: DF scattering images of different nanocavities after UV illumination. Curved lines are fitted with Lorentz peak model. (c) Resonant energy of nanocavities, *chla*, and hybrid modes as a function of extracted detuning. The horizontal line indicates the resonant energy of exciton, the black dots are carried out from Fig. 2b. (d) Coupling strength g versus the detuning between the nanocavities and *chla* resonance. The blue line denotes the averaged value of coupling strength g .

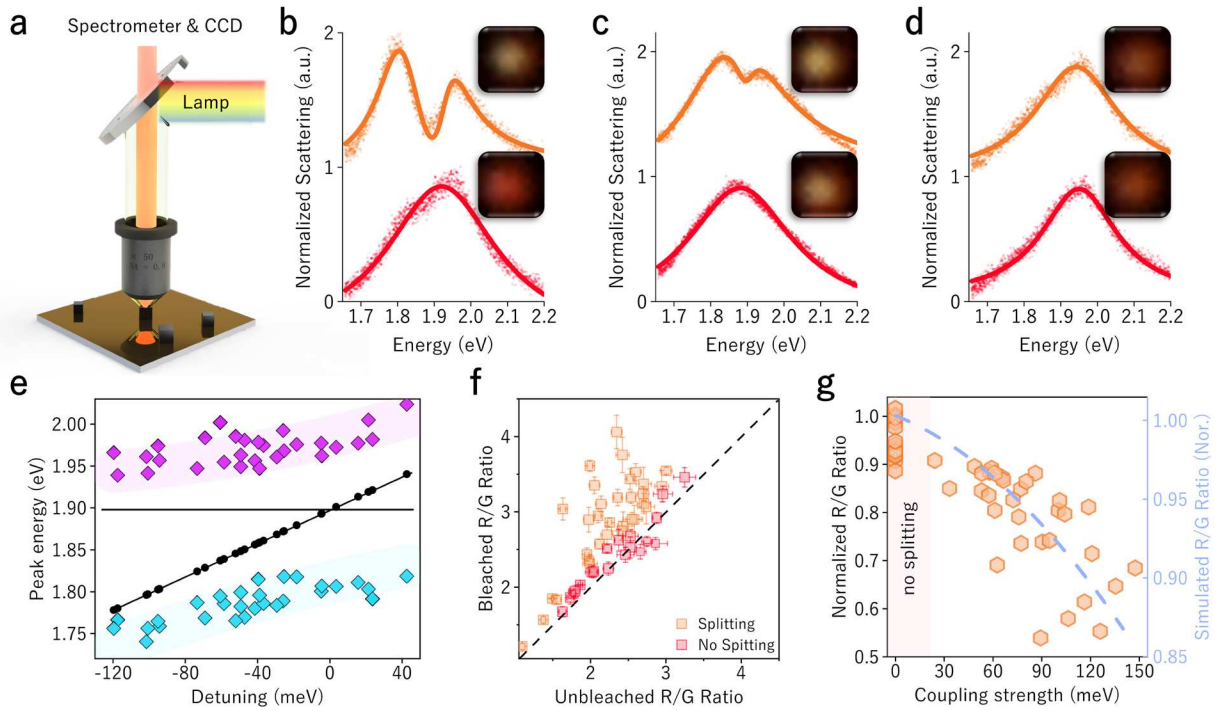


Figure 3. Color change of DF image as a function of coupling strength. (a) Optical system illustration of DF spectra and image collection. (b-d) Normalized scattering spectra of nanocavities coupled with *chla* molecules before (top) and after (bottom) photobleaching process (UV illumination). Inset CCD images: DF image of nanocavities coupled with *chla* molecules before (top) and after (bottom) photobleaching process. (b) strong coupling; (c) intermediate coupling; (d) weak coupling. (e) Resonant energy of nanocavities, *chla*, and hybrid modes as a function of extracted detuning value. (f) The ratio between the red to green channel (R/G ratio) extracted from DF images before and after photobleaching. The black dot line represents the R/G ratio remains the same after photobleaching. Error bars were based on 3 nanocubes. (g) Left: normalized R/G ratio as a function of coupling strength g . Right: simulated normalized R/G ratio according to the two coupled oscillators model and CCD efficiency at different wavelengths.

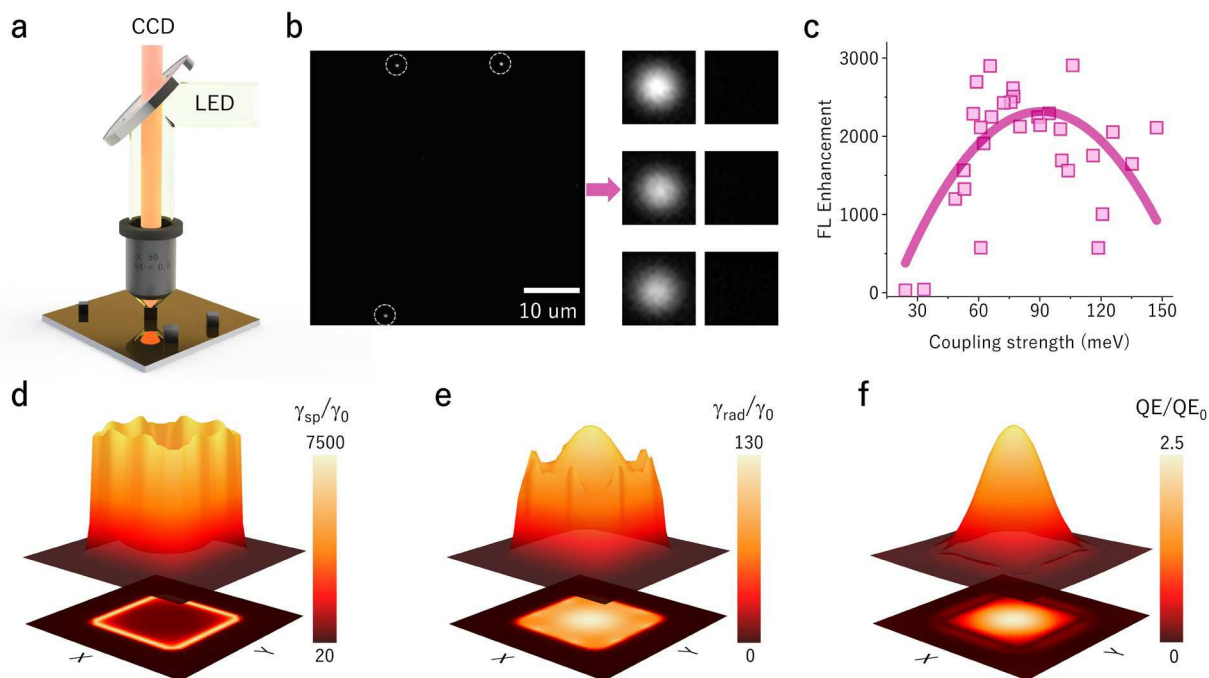


Figure 4. FL enhancement as a function of coupling strength (a) Optical system illustration of FL image collection. (b) Left: representative FL image of nanocavities coupled with *chla* molecules. Right: enlarged FL images of nanocavities and background. (c) FL enhancement factor $\langle EF \rangle$ as a function of coupling strength. The pinkish curve denotes the quadratic fitting. (d-f) Maps of enhancement of the spontaneous emission rate (Purcell factor) (d), enhancement of radiative emission rate (e), and enhancement of dipole quantum efficiency (f) as a function of dipole position under Ag nanocube. The dipole located at the gap between the Ag nanocube and the gold mirror is vertically oriented (0° relative to the surface normal z -axis).

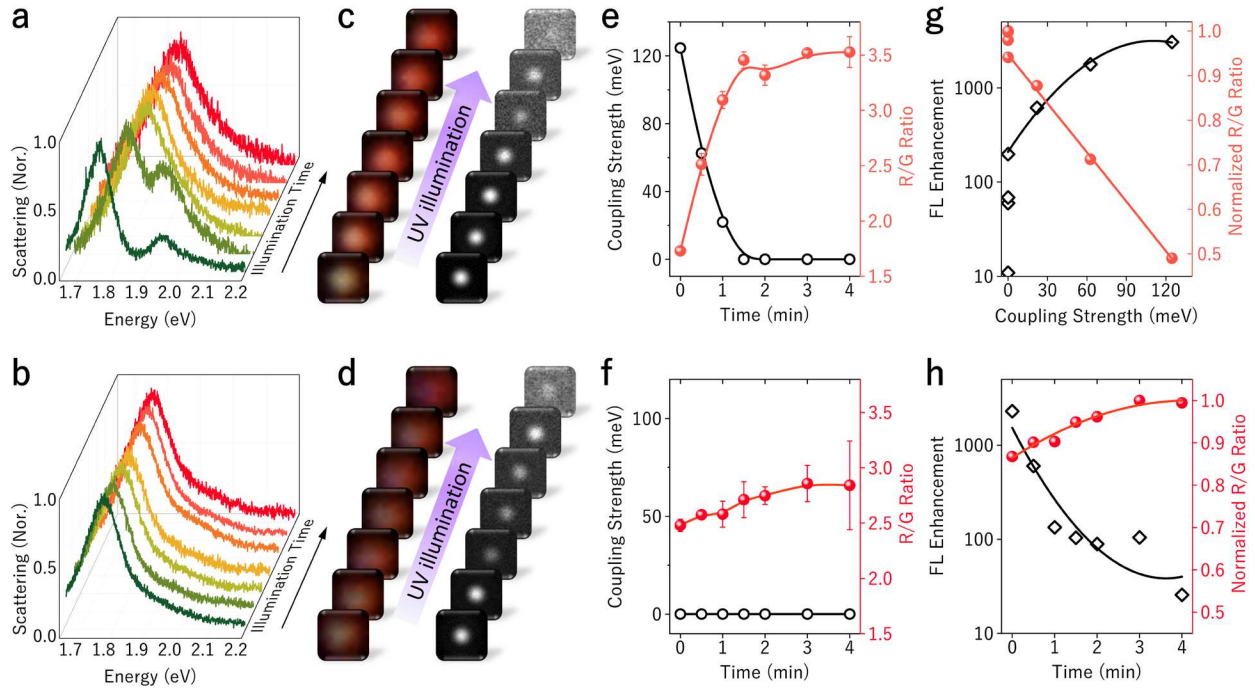


Figure 5. Evolution of far-field images during the photobleaching. (a-b) Dynamic changes of the DF spectra of *chla*-coupled nanocavities under (a) strong and (b) weak coupling regimes. Illumination of UV light was shined to change the number of excitons. The collection time are 0 min, 0.5 min, 1min, 1.5 min, 2 min, 3 min, and 4 min. (c-d) Evolution of the DF and FL image of *chla* coupled nanocavities corresponding to (a) and (b). (e-f) Coupling strength and R/G ratio as a function of UV illumination time. (g) Normalized R/G ratio and $\langle EF \rangle$ as a function of coupling strength extracted from (a) and (c). The black curve line and orange curve line denote the quadratic fitting. (h) Normalized R/G ratio and $\langle EF \rangle$ as a function of UV illumination time extracted from (b) and (d). Error bars are produced by 4 data.

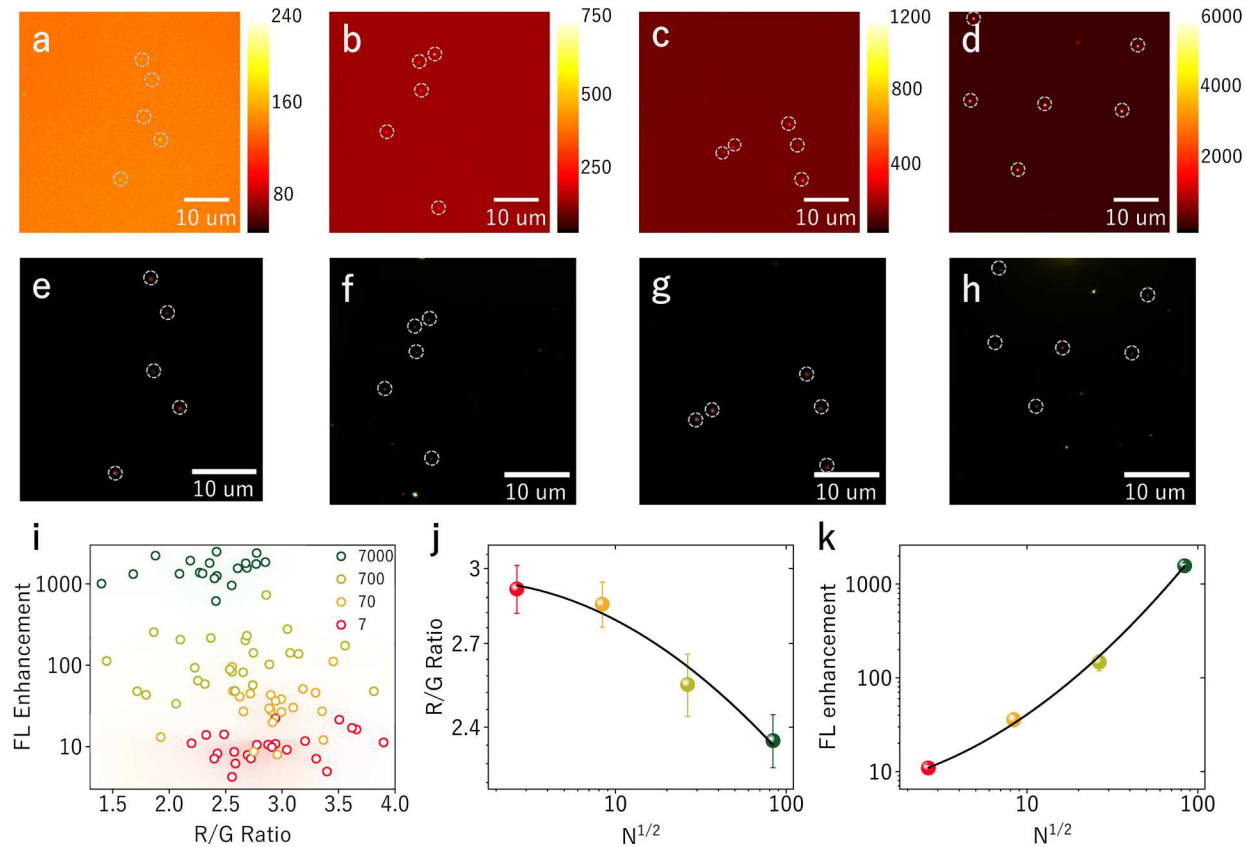


Figure 6. Demonstration of quantitative capability of far-field imaging. (a-d) Representative fluorescence microscopic images of multiple nanocavities containing (a) 7, (b) 70, (c) 700, and (d) 7000 *chla* molecules between the gold mirror and nanocube. (e-h) Corresponding dark field images of nanocavities containing (e) 7, (f) 70, (g) 700, and (h) 7000 *chla* molecules between the gold mirror and nanocube. Each dashed circle represents an independent single nanocube. (i) R/G ratio and $\langle EF \rangle$ distribution of *chla* coupled nanocavities containing different number of *chla* molecules. Background color maps are generated by kernel density matrix. (j) R/G ratio versus the square root of *chla* number. The black curve line denotes the quadratic fitting. (k) $\langle EF \rangle$ versus the square root of *chla* number. The black curve line denotes the quadratic fitting.

Supplementary Files

This is a list of supplementary files associated with this preprint. Click to download.

- [SupplementaryInformationsubmission.pdf](#)